Dynamics of the perceived velocity gradient tensor and its modelling

Ping-Fan Yang ◉,[1,2,3] Eberhard Bodenschatz,[4] Guo Wei He,[1,2]
Alain Pumir,[5,4,*] and Haitao Xu ◉[3,†]

[1]*The State Key Laboratory of Nonlinear Mechanics, Institute of Mechanics, Chinese Academy of Sciences, Beijing 100190, China*
[2]*School of Engineering Sciences, University of Chinese Academy of Sciences, Beijing 100049, China*
[3]*Center for Combustion Energy and School of Aerospace Engineering, Tsinghua University, 100084 Beijing, China*
[4]*Max-Planck Institute for Dynamics and Self-Organisation, Göttingen D-37077, Germany*
[5]*Laboratoire de Physique, Ecole Normale Supérieure de Lyon and CNRS, F-69007 Lyon, France*

We study the dynamics of the perceived velocity gradient tensor **M** constructed from four tracer particles that initially form a regular tetrad of size r_0. The exact evolution equation of **M**, derived in our previous work [Yang *et al.*, J. Fluid Mech. **897**, A9 (2020)], contains several unclosed terms. Using numerical data, we compare the exact dynamics of **M** with the tetrad model [Chertkov *et al.*, Phys. Fluids **11**, 2394 (1999)]. In particular, we project the motion onto the (R, Q) plane, where R and Q are the third- and second-order invariants of **M**. When r_0 is in the inertial range of scales of the turbulent cascade, we find that at very short times the tetrad model correctly describes the main features of the dynamics of **M** on the (R, Q) invariants plane. This suggests that at any instant of time, the unclosed pressure and viscous contributions to the Eulerian dynamics of **M** could be described by the nonlinear and the damping terms, respectively, in the tetrad model. However, after a time of order $\sim 2\tau_K$, where τ_K is the Kolmogorov timescale, the action of the unclosed pressure contribution to the dynamics changes very dramatically to become a strong damping term on the (R, Q) plane. This qualitative change in the dynamics occurs on a timescale that differs from T_0, the turnover time at scale r_0. In addition, the fluctuations around the mean are found to deviate from the short-correlated-white-noise assumption in the tetrad model, as the timescale of the fluctuation is closer to T_0 than τ_K.

I. INTRODUCTION

Understanding the dynamics of the coarse-grained velocity gradient tensor in a turbulent flow is a prerequisite to accurately describe and model flows in numerous engineering and natural situations, in which the whole range of scales of turbulent motion cannot be fully resolved. The velocity gradient tensor, $\tilde{\mathbf{M}}$, coarse-grained over a size r_0, is an indispensable ingredient in the modeling of turbulent flows in complex situations [1–6]. Providing a description of the statistical properties of $\tilde{\mathbf{M}}$ and understanding its evolution has been the subject of numerous studies [1,7–9]. A convenient approximation to the coarse-grained velocity gradient tensor is the perceived velocity-gradient tensor (PVGT), **M**, constructed with the help of four points forming initially a regular tetrad of size

---

*alain.pumir@ens-lyon.fr

†hxu@mail.tsinghua.edu.cn

r_0. Although $\mathbf{M}$ differs from the coarse-grained velocity gradient tensor $\tilde{\mathbf{M}}$, it provides a surrogate to study its dynamics.

Importantly, the evolution of $\mathbf{M}$ is sensitive to one of the essential features of turbulent flows, which consists in modifying the relative distance between tracers following the flow, and strongly distorting the shape defined by a set of particles [10–13]. The underlying motion can be analyzed in terms of rotation, compression, and stretching in different directions, with very fast dynamics [7–9]. Additionally, $\mathbf{M}$ provides a characterization of the flow properties at the scale r_0. In fact, turbulent fluid motion at very high Reynolds numbers involves a wide range of spatial inertial scales, where neither the influences of forcing, acting at large scales, nor of viscosity, acting at small scales, play a significant role [14,15]. In a statistically steady state, the amount of energy supplied by the forcing is simply transferred through the inertial range, with an energy flux ε, equal to the viscous dissipation of kinetic energy. Describing quantitatively the velocity fluctuations over the inertial range of scales is notoriously challenging. The theoretical difficulties originate both from the nonlinearities in the Navier-Stokes equations and from the nonlocal character of the pressure term. In the case of the PVGT, the dynamics of the alignment of vorticity, defined from the antisymmetric part of $\mathbf{M}$, with the eigenvectors of strain, defined by the symmetric part of $\mathbf{M}$, can be understood as a result of the deformation of tetrads and of the conservation of angular momentum [8,9]. We consider here the dynamics occurring over a shorter timescale when the deformation of the tetrads remains limited.

Contrary to the velocity gradient tensor itself, the perceived velocity gradient $\mathbf{M}$ is not traceless. This implies that it must be described by a 3×3 matrix. Of the resulting 9 degrees of freedom of $\mathbf{M}$, 3 correspond to an overall rotation of the coordinate system and is therefore not so relevant dynamically. In the corresponding high-dimensional space, it is convenient to project the dynamics on a reduced set of variables, which are invariant under a change of coordinates. A classical choice consists of P, Q, and R, where $P \equiv -\text{tr}(\mathbf{M})$, $Q \equiv -\frac{1}{2}\text{tr}(\hat{\mathbf{M}}^2)$, and $R \equiv -\frac{1}{3}\text{tr}(\hat{\mathbf{M}}^3)$, with $\hat{\mathbf{M}} = \mathbf{M} + \frac{1}{3}P\mathbf{I}$ being the traceless part of $\mathbf{M}$ and $\mathbf{I}$ being the identity tensor. The invariants Q and R completely determine the eigenvalues of $\hat{\mathbf{M}}$ by the characteristic polynomial $X^3 + QX + R = 0$. In particular, when the values of Q and R satisfy $\Delta = 4Q^3 + 27R^2 < 0$, the three eigenvalues of $\hat{\mathbf{M}}$ are all real, whereas when $\Delta > 0$, $\hat{\mathbf{M}}$ has two complex conjugate eigenvalues and a real one. The invariants R and Q, therefore, provide essential insight into the local topology of the flow.

One of the ideas proposed to model the evolution of $\mathbf{M}$ can be traced back to the very simple closure proposed by Vieillefosse [16,17], who postulated an isotropic form for the second derivatives (Hessian) of pressure. The resulting restricted Euler (RE) approximation leads to a set of ordinary differential equations that can be exactly solved [17,18]. The variables Q and R diverge at a finite time, along the separatrix $\Delta = 0$ ($R \to \infty$). Although this divergence is an artifact of the simplifications of the problem, the RE approximation correctly captures a tendency of (R, Q) to drift along the separatrix $\Delta = 0$, towards $R > 0$, an effect clearly shown in the joint probability distribution function (PDF) of R and Q in turbulent flows [19,20] and further investigated theoretically [1,21,22].

In this work, we use the approach based on tetrads, which rests on determining the perceived velocity gradient tensor (PVGT) from the motion of four tracer particles, initially forming a regular tetrad [7,8]. To characterize the evolution of $\hat{\mathbf{M}}$ in terms of the invariants R and Q, we rely on the exact evolution equation of $\mathbf{M}$ derived in our previous work [23]:

$$\frac{d\mathbf{M}}{dt} = -\mathbf{M}^2 + \mathbf{\Pi} \cdot \mathbf{H}^p + \mathbf{\Pi} \cdot \mathbf{H}^\nu + \mathbf{\Pi} \cdot \mathbf{H}^f, \qquad (1)$$

where $\mathbf{H}^p$, $\mathbf{H}^\nu$, and $\mathbf{H}^f$ denote the pressure, viscosity, and forcing contributions to the dynamics of $\mathbf{M}$, and $\mathbf{\Pi}$ is a shape-dependent tensor, which reduces to unity when the tetrad is regular [23].

The present paper is organized as follows. In Sec. II A we summarize the main steps and concepts introduced to derive Eq. (1). Then in Sec. II B we review the tetrad model proposed in Ref. [7]. Next, in Sec. III, we will determine the evolution of R and Q conditioned on the initial values (R_0, Q_0) and show that the dynamics at $t = 0$ can be approximately described by the tetrad model. We will see that at $t = 0$, the pressure term $\mathbf{\Pi}\mathbf{H}^p$ counteracts the nonlinear term in the equation of $\hat{\mathbf{M}}$ and

can be modelled by the nonlinear α term in tetrad model, i.e., $\alpha[\hat{\mathbf{M}}^2 - \mathbf{\Pi}\mathrm{tr}(\hat{\mathbf{M}}^2)]$ [7], while the viscous part $\mathbf{\Pi}\mathbf{H}^\nu$ could be well described by the damping ζ term, $\zeta\hat{\mathbf{M}}$ [7]. However, a very short time later [$t \lesssim 0.1T_0$, where $T_0 \equiv (r_0^2/\varepsilon)^{1/3}$ and ε is the dissipation rate], $\mathbf{\Pi}\mathbf{H}^p$ behaves more like a strong damping term and the mean trajectories above the Vieillefosse tail on the (R, Q) plane move towards the origin. Furthermore, at $t = 0$ those terms related to P are negligible in the equations of Q and R, yet soon after they play a role, at least in part of the (R, Q) plane. We will see that actually in addition to T_0, the dissipative timescale $\tau_K \equiv (\nu/\varepsilon)^{1/2}$ also enters the dynamics of $\mathbf{M}$. Moreover, we characterize the fluctuations of R and Q around the mean trajectories. We find that the fluctuations around the mean trajectories deviate from the white-noise assumption, which has been proposed previously in the tetrad model [7]; instead, the correlation timescale of the fluctuations is more likely to be T_0.

II. THEORETICAL BACKGROUND

In this section we first recall the derivation of the exact evolution equations for the invariants Q and R of the PVGT in the case of homogeneous and isotropic turbulence (HIT), and then we will compare them with the tetrad model.

A. Exact evolution equations of PVGT on the invariants plane

We start with the definition of PVGT. Following previous works [8,9], considering four fluid particles in a homogeneous and isotropic flow, we compute the PVGT $\mathbf{M}$ as follows. Denoting the positions and velocities of the four points in the laboratory frame by $\mathbf{X}^\alpha$ and $\mathbf{U}^\alpha$, ($\alpha = 1, 2, 3, 4$), respectively, we introduce the coordinates $\mathbf{x}^\alpha$ with respect to the center of mass, $\mathbf{x}^\alpha = \mathbf{X}^\alpha - \mathbf{X}^0$, where $\mathbf{X}^0 = \frac{1}{4}\sum_{\alpha=1}^4 \mathbf{X}^\alpha$, and the reduced velocity, $\mathbf{u}^\alpha$, $\mathbf{u}^\alpha = \mathbf{U}^\alpha - \mathbf{U}^0$, where $\mathbf{U}^0 = \frac{1}{4}\sum_{\alpha=1}^4 \mathbf{U}^\alpha$. The perceived velocity gradient tensor $\mathbf{M}$, based on the four points of the tetrahedron, is defined by

$$x_j^\alpha M_{ji} = u_i^\alpha \qquad \text{for} \quad \alpha = 1, 2, 3, 4, \tag{2}$$

or, equivalently, after multiplying both terms of Eq. (2) by x_k^α and summing over α:

$$M_{ij} = g_{ik}^{-1} \Xi_{kj}, \tag{3}$$

where the tensors $\mathbf{g}$ and $\mathbf{\Xi}$ are defined by

$$g_{ij} \equiv \sum_{\alpha=1}^4 x_i^\alpha x_j^\alpha \quad \text{and} \quad \Xi_{ij} \equiv \sum_{\alpha=1}^4 x_i^\alpha u_j^\alpha. \tag{4}$$

Unlike the true velocity gradient tensor $m_{ij} \equiv \frac{\partial U_i}{\partial x_j}$, the trace of $\mathbf{M}$, $\mathrm{tr}(\mathbf{M})$ is in general nonzero. Following the previous works [7], in the rest of the text we will focus on the invariants of the traceless part of $\mathbf{M}$, $\hat{\mathbf{M}}$, and the independent invariants of $\hat{\mathbf{M}}$: $Q \equiv -\frac{1}{2}\mathrm{tr}(\hat{\mathbf{M}}^2)$ and $R \equiv -\frac{1}{3}\mathrm{tr}(\hat{\mathbf{M}}^3)$.

The exact yet unclosed equation for the evolution of $\mathbf{M}$ reads [23]:

$$\frac{d\mathbf{M}}{dt} = -\mathbf{M}^2 + \mathbf{\Pi}\mathbf{H},$$

where $\mathbf{\Pi} \equiv \frac{\mathbf{g}^{-1}}{\mathrm{tr}(\mathbf{g}^{-1})}$ is the shape factor [7] and the driving term $\mathbf{H}$ is defined by

$$H_{ij} = \mathrm{tr}(\mathbf{g}^{-1}) \sum_{\alpha=1}^4 x_i^\alpha a_j^\alpha. \tag{5}$$

In Eq. (5), $\mathbf{a}^\alpha$ is the accelerations of fluid particle α relative to the center of mass, which is related to the acceleration in the laboratory frame $\mathbf{A}^\alpha$ by $\mathbf{a}^\alpha = \mathbf{A}^\alpha - \frac{1}{4}\sum_{\beta=1}^4 \mathbf{A}^\beta$. The Navier-Stokes equations

express that

$$\mathbf{A}^\alpha = \frac{d\mathbf{U}^\alpha}{dt} = -\boldsymbol{\nabla} p^\alpha + \mathbf{F}^\alpha + \nu\nabla^2\mathbf{U}^\alpha, \tag{6}$$

where p denotes the pressure and $\mathbf{F}$ is the external body force per unit mass. Thus the driving term H_{ij} can be decomposed into H_{ij}^p, H_{ij}^ν, and H_{ij}^f, which represent the contributions to H_{ij} from the pressure gradient, the viscous forces, and the external forcing, respectively. Now the equation for $\hat{\mathbf{M}}$ could be readily derived from Eq. (5). Taking the trace of Eq. (5) yields:

$$\frac{d\,\mathrm{tr}(\mathbf{M})}{dt} = -\mathrm{tr}(\mathbf{M}^2) + \mathrm{tr}(\boldsymbol{\Pi}\mathbf{H})$$

$$= -\left[\mathrm{tr}(\hat{\mathbf{M}}^2) + \frac{1}{3}\mathrm{tr}(\mathbf{M})^2\right] + \mathrm{tr}(\boldsymbol{\Pi}\mathbf{H}), \tag{7}$$

where we have used the relation $\mathrm{tr}(\mathbf{M}^2) = \mathrm{tr}[(\hat{\mathbf{M}} + \frac{1}{3}\mathrm{tr}(\mathbf{M})\,\mathbf{I})^2] = \mathrm{tr}(\hat{\mathbf{M}}^2) + \frac{1}{3}\mathrm{tr}(\mathbf{M})^2$. Subtracting Eq. (7) from Eq. (5) yields:

$$\frac{d\hat{M}_{ij}}{dt} + \hat{M}_{ik}\hat{M}_{kj} - \frac{1}{3}\hat{M}_{mn}\hat{M}_{nm}\delta_{ij} + \frac{2}{3}M_{kk}\hat{M}_{ij} = \Pi_{ik}H_{kj} - \frac{1}{3}\Pi_{mn}H_{nm}\delta_{ij}, \tag{8}$$

or in the matrix form as

$$\frac{d\hat{\mathbf{M}}}{dt} + \hat{\mathbf{M}}^2 - \frac{1}{3}\mathrm{tr}(\hat{\mathbf{M}}^2)\mathbf{I} + \frac{2}{3}\mathrm{tr}(\mathbf{M})\hat{\mathbf{M}} = \boldsymbol{\Pi}\mathbf{H} - \frac{1}{3}\mathrm{tr}(\boldsymbol{\Pi}\mathbf{H})\mathbf{I}. \tag{9}$$

The equations for the invariants P, Q and R can be easily derived from Eqs. (8) or (9):

$$\frac{dP}{dt} = -2Q + \frac{1}{3}P^2 - \mathrm{tr}(\boldsymbol{\Pi}\mathbf{H})\,, \tag{10}$$

$$\frac{dQ}{dt} = -3R + \frac{4}{3}PQ - \mathrm{tr}(\hat{\mathbf{M}}\hat{\mathbf{H}})\,, \tag{11}$$

$$\frac{dR}{dt} = \frac{2}{3}Q^2 + 2PR - \mathrm{tr}(\hat{\mathbf{M}}^2\hat{\mathbf{H}})\,, \tag{12}$$

where

$$\hat{\mathbf{H}} \equiv \boldsymbol{\Pi}\mathbf{H} - \tfrac{1}{3}\mathrm{tr}(\boldsymbol{\Pi}\mathbf{H})\mathbf{I}, \tag{13}$$

is the traceless part of $\boldsymbol{\Pi}\mathbf{H}$, which can also be decomposed as sum of three contributions, due to forcing, $\hat{\mathbf{H}}^f$, to pressure, $\hat{\mathbf{H}}^p$, and to viscosity, $\hat{\mathbf{H}}^\nu$, in parallel to the decomposition of $\mathbf{H}$ in Eqs. (5) and (6). The tensor $\hat{\mathbf{H}}$ is unclosed, in the sense that it cannot be determined from the knowledge of $\hat{\mathbf{M}}$ alone. We notice that $-P$, the trace of $\mathbf{M}$, is also an unclosed quantity. To proceed we need to model the unclosed terms. The tetrad model [7] proposes a strategy to describe the unclosed terms, which we will review in the following subsection.

B. The tetrad model

The main difficulty in modeling the equations of motion comes from the nonlocal pressure Hessian term. Neglecting forcing and viscosity, the equation for the true velocity gradient $\mathbf{m}$, defined by $m_{ij} = \partial_j u_i$, where $\mathbf{u}$ is the fluctuating velocity field, reduces to

$$\frac{d}{dt}m_{ij} + m_{ik}m_{kj} = -\partial_i\partial_j p\,, \tag{14}$$

where d/dt represents the Lagrangian derivative $\frac{d}{dt} = \frac{\partial}{\partial t} + u_j\frac{\partial}{\partial x_j}$. The incompressibility condition requires that pressure satisfies a Poisson equation, $\nabla^2 p + \mathrm{tr}(\mathbf{m}^2) = 0$. This shows the nonlocal

character of pressure, which is a major source of difficulty. The RE closure [17] simply postulates an isotropic form for the pressure Hessian: $\partial_{ij}p = -\text{tr}(\mathbf{m}^2)\delta_{ij}/3$.

Based on phenomenological considerations, the following set of stochastic differential equations has been proposed by Chertkov *et al.* [7] to describe the evolution of the PVGT $\mathbf{M}$ with the implicit assumption that $\text{tr}(\mathbf{M}) = 0$ and thus $\mathbf{M} = \hat{\mathbf{M}}$:

$$\frac{d\hat{\mathbf{M}}}{dt} + \hat{\mathbf{M}}^2 - \mathbf{\Pi}\,\text{tr}(\hat{\mathbf{M}}^2) = \alpha[\hat{\mathbf{M}}^2 - \mathbf{\Pi}\text{tr}(\hat{\mathbf{M}}^2)] - \zeta\hat{\mathbf{M}} + \boldsymbol{\eta}, \tag{15}$$

in which α is a dimensionless coefficient assumed to be universal when r_0 is in the inertial range of scales, i.e., flow independent and $\boldsymbol{\eta}$ is a random tensor representing the fluctuations of the dynamics of $\hat{\mathbf{M}}$ due to scales smaller than r_0. Note that the damping term $-\zeta\mathbf{M}$ was not considered in Ref. [7] and will be discussed below. It should be pointed out that the tetrad model, Eq. (15), implies that the dynamics of $\hat{\mathbf{M}}$ evolves with the timescale T_0, which is also the basic assumption adopted by almost all models dealing with the inertial range dynamics of turbulence, see, e.g., a model on the relative dispersion of multiple fluid tracers [24]. A straightforward comparison between Eq. (15) and Eq. (9) reveals that the first two terms on the left-hand side are exactly the same. The third term on the left-hand side of Eq. (15) is obtained by replacing the tensor $\frac{1}{3}\mathbf{I}$ in the RE equation by $\mathbf{\Pi}$. This coupling satisfies the condition that pressure does not do any work in homogeneous isotropic flows [7]. Although $\mathbf{\Pi}$ reduces to $\frac{1}{3}\mathbf{I}$ when the tetrads are regular, the coupling is significantly affected when the tetrahedra are strongly distorted. When the tetrahedra are regular with side length r_0, however, $\mathbf{g} = \frac{r_0^2}{2}\mathbf{I}$ and $\mathbf{\Pi} = \frac{1}{3}\mathbf{I}$, so the two tensors do not differ much as long as one focuses on short timescales or, equivalently, when the deformation is not too strong. Another source of difference between the tetrad model and the exact equation comes from the absence of $\text{tr}(\mathbf{M})$ in Eq. (15); see the fourth term on the left-hand side of Eq. (9). Although we will check that this term is negligible at $t = 0$, it does play a role very soon after the start of tetrahedron deformation. Finally, a comparison of the terms on the right-hand side of Eq. (9) and (15) suggests that the three elements introduced in the tetrad model, namely the α, ζ, and $\boldsymbol{\eta}$ terms, correspond to the unclosed $\hat{\mathbf{H}}$ term in the exact equation. In fact, the α term represents the reduction of nonlinearity effect $\propto \hat{\mathbf{M}}^2$ by a factor $(1 - \alpha)$ [2,7]. In the dissipative range, when $r_0 \lesssim \eta_K$, where $\eta_K \equiv (\nu^3/\varepsilon)^{1/4}$ is the Kolmogorov length scale, the effect of the pressure Hessian on the dynamics of true velocity gradient tensor could be partially understood, using a Gaussian approximation, by the "suppression of nonlinearity" phenomenology [25]. Thus if we generalize this idea to $r_0 \gtrsim \eta_K$, then we could regard the α term as a model for the pressure part of $\hat{\mathbf{H}}$, i.e., $\hat{\mathbf{H}}^p$.

The term $\zeta\hat{\mathbf{M}}$ is a damping term, with a coefficient ζ with the dimension of the inverse of a time, and likewise, it could be thought of as a model for the viscous contribution $\hat{\mathbf{H}}^\nu$, as shown in Refs. [25,26] for the true VGT. One of the important question concerns the scaling of ζ with the scale of the tetrad, r_0. We will test here the reasonable assumption that the characteristic timescale of evolution of the tetrad is $T_0 = (r_0^2/\varepsilon)^{1/3}$. The stochastic terms, $\boldsymbol{\eta}$, proposed to represent the effects of the small-scale jitter on the evolution of $\hat{\mathbf{M}}$, is modelled by a white-in-time, Gaussian noise, whose variance scales as ε/r_0^2, consistent with Kolmogorov theory [15]:

$$\langle\eta_{ab}(0)\eta_{cd}(t)\rangle = \frac{2C_\eta\varepsilon}{r_0^2}\left(\delta_{ac}\delta_{bd} - \frac{1}{3}\delta_{ab}\delta_{cd}\right) \times \delta(t), \tag{16}$$

where C_η is an unknown constant.

If we restrict ourselves to the short-time evolution of initially regular tetrahedra when $\mathbf{\Pi}$ is close to $\frac{1}{3}\mathbf{I}$, then the model equations for the invariants R and Q read:

$$\frac{dQ}{dt} + 3(1-\alpha)R + 2\zeta Q = -\text{tr}(\boldsymbol{\eta}\hat{\mathbf{M}}), \tag{17}$$

$$\frac{dR}{dt} - (1-\alpha)\frac{2Q^2}{3} + 3\zeta R = -\text{tr}(\boldsymbol{\eta}\hat{\mathbf{M}}^2). \tag{18}$$

This formulation helps us understand the exact dynamics of R and Q [cf. Eqs. (11) and (12)]. The terms on the right-hand side of Eqs. (18) and (17) correspond to Gaussian noise, with a zero mean and with a variance that can be readily computed from Eq. (16). A comparison of the evolution of R and Q in turbulent flows with the model prediction allows one to check the quality of the modeling proposed. The α and ζ terms in the model, which are interpreted as resulting from the pressure and viscosity, respectively, can be determined by averaging $\frac{dR}{dt}$, $\frac{dQ}{dt}$ conditioned on R and Q, effectively averaging out the fluctuations. Subsequently, the structure of the stochastic term $\boldsymbol{\eta}$ can be investigated by studying the fluctuations of the trajectories relative to the conditional averages on the (R, Q) plane.

In the next section, we will characterize the dynamics with the help of direct numerical simulations (DNS) data. This will help us understand the shortcomings of the model.

III. NUMERICAL RESULTS AND DISCUSSION

In order to investigate the behavior of PVGT on the (R, Q) invariants plane, and compare the tetrad model with the exact dynamics, we rely on data from DNS.

A. Databases

We used here the dataset "Forced isotropic turbulence" from the Johns Hopkins turbulence database (JHTDB) with 1024^3 grids and $R_\lambda = 433$ [27]. We organized the downloaded data into two datasets for Eulerian and Lagrangian statistics, respectively.

The Eulerian dataset (Set E) contains a set of velocity and acceleration at 512^3 data points from one single snapshot similar to the data set used in our previous work [23]. Since four points out of the eight vertices of a cube form a regular tetrahedron, the smallest tetrad size $r_{0,\min}$ that can be obtained from the 512^3 points is $\sqrt{2}$ times the grid spacing. Tetrads with sizes multiple of $r_{0,\min}$ can also be obtained without interpolation [23]. For Set E, the value of $r_{0,\min}$ is $r_{0,\min} \approx 6.3\eta_K$.

The Lagrangian dataset (Set L) consists of Lagrangian trajectories, obtained by using the Lagrangian tracking function "GetPosition" [28] of the JHTDB to follow the motion of tracer particles. We started from eight snapshots and followed the motion of 128^3 points at each snapshot, from which we could construct the evolution of PVGT. For Set L, $r_{0,\min} \approx 25.2\eta_K$ and the number of Lagrangian trajectories of initially regular tetrads is $8 \times 128^3 \approx 1.68 \times 10^7$.

B. The unclosed pressure and viscosity terms and their modeling

The terms involving $\mathbf{H}$ are all unclosed in Eqs. (11) and (12). In this section, we discuss the modeling of these terms, using our numerical database. Specifically, the analysis presented below rests on the dataset E.

In the case of the true velocity gradient $\mathbf{m}$, Ref. [25] established, using a joint Gaussian distribution assumption of the velocity increments, that the viscous term $\nu\nabla^2\mathbf{m}$ conditioned on velocity gradient $\mathbf{m}$ could be modeled by a linear damping (or linear diffusion) term, and the contribution from pressure Hessian could be modeled by a nonlinear model term. The former conclusion about the viscous term was also obtained in Ref. [26]. These results suggest that in the tetrad model, the nonlinear α term, and the linear ζ term in Eq. (15) could correspond to the $\mathbf{H}^p$ and the $\mathbf{H}^\nu$ terms in the exact equation (9), respectively. We also note that while α is dimensionless, ζ has the dimension of the inverse of a time. A direct comparison between Eqs. (11) and (17) and between Eqs. (12) and (18) provides the following relation between fluctuating quantities:

$$-3\,\alpha\,R = \mathrm{tr}(\hat{\mathbf{M}}\hat{\mathbf{H}}^p) + \text{fluctuations}, \tag{19}$$

$$2\,\zeta\,Q = \mathrm{tr}(\hat{\mathbf{M}}\hat{\mathbf{H}}^\nu) + \text{fluctuations}, \tag{20}$$

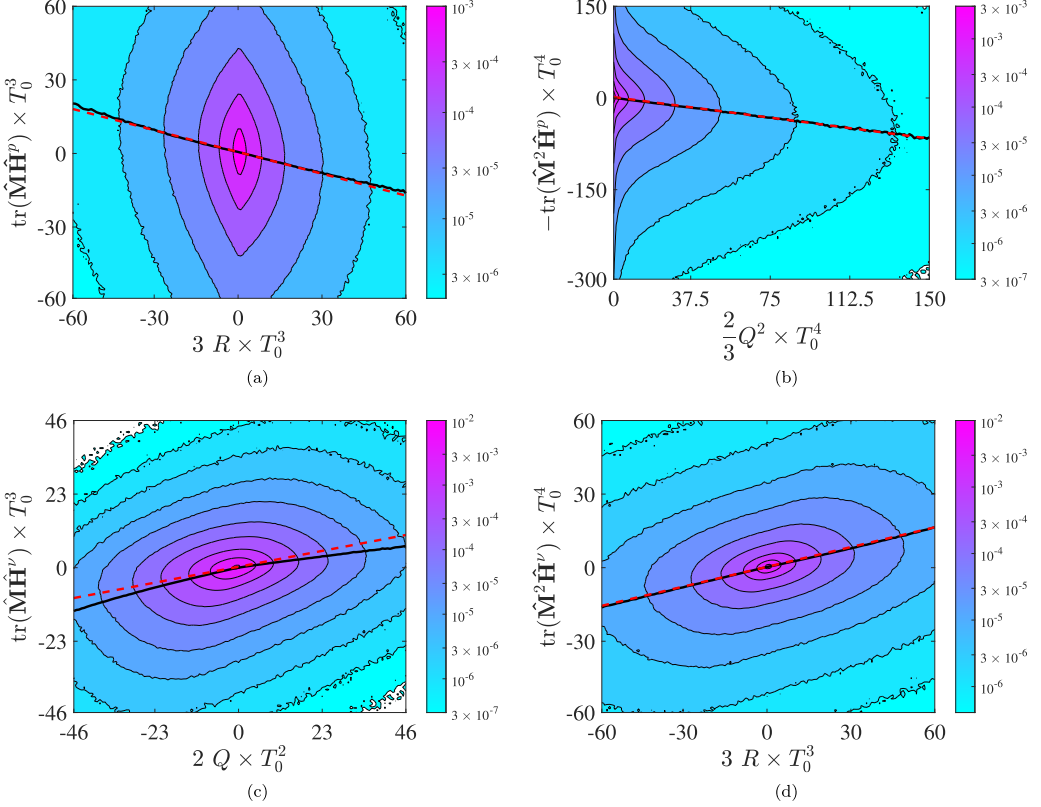$$-\tfrac{2}{3}\,\alpha\,Q^2 = -\mathrm{tr}(\hat{\mathbf{M}}^2\hat{\mathbf{H}}^p) + \text{fluctuations}, \tag{21}$$

FIG. 1. Joint PDFs between (a) $3R$ and $\text{tr}(\hat{\mathbf{M}}\hat{\mathbf{H}}^p)$, (b) $\frac{2}{3}Q^2$ and $-\text{tr}(\hat{\mathbf{M}}^2\hat{\mathbf{H}}^p)$, (c) $2Q$ and $\text{tr}(\hat{\mathbf{M}}\hat{\mathbf{H}}^v)$, and (d) $3R$ and $\text{tr}(\hat{\mathbf{M}}^2\hat{\mathbf{H}}^v)$ for regular tetrahedra, with size $r_0 \approx 100\eta_K$ at $t = 0$. All quantities are normalized by T_0. The black solid curves are the conditional averages of ordinates conditioned on abscissas, and the red dashed lines are the linear fitting. Please note that in (a) and (b), we followed the same convention as in Ref. [2] so that a negative slope of the red dashed line means a positive value of α.

$$3\,\zeta\,R = \text{tr}(\hat{\mathbf{M}}^2\hat{\mathbf{H}}^v) + \text{fluctuations}, \tag{22}$$

in which the fluctuations terms in each equation above represent the contributions due to the scales of motion below r_0, the tetrad size. If we assume that the fluctuations are independent of R and Q, then the averaged quantities above, conditioned on R or Q become

$$-3\,\alpha_R\,R = \langle\text{tr}(\hat{\mathbf{M}}\hat{\mathbf{H}}^p)|R\rangle, \tag{23}$$

$$2\,\zeta_Q\,Q = \langle\text{tr}(\hat{\mathbf{M}}\hat{\mathbf{H}}^v)|Q\rangle, \tag{24}$$

$$-\tfrac{2}{3}\,\alpha_Q\,Q^2 = -\langle\text{tr}(\hat{\mathbf{M}}^2\hat{\mathbf{H}}^p)|Q\rangle, \tag{25}$$

$$3\,\zeta_R\,R = \langle\text{tr}(\hat{\mathbf{M}}^2\hat{\mathbf{H}}^v)|R\rangle, \tag{26}$$

where α_Q and α_R are the values of α obtained by conditioning on Q and R, respectively, and ζ_Q and ζ_R are obtained similarly. The formulation of the tetrad model, see Sec. II B, assumes that the two sets of parameters are identical: $\alpha_Q = \alpha_R$ and $\zeta_Q = \zeta_R$.

The DNS results provide partial support to this view. Following Fig. 17 of Ref. [2], Fig. 1 shows the joint PDFs between the pressure or viscous terms in Eqs. (11) and (12), and the corresponding
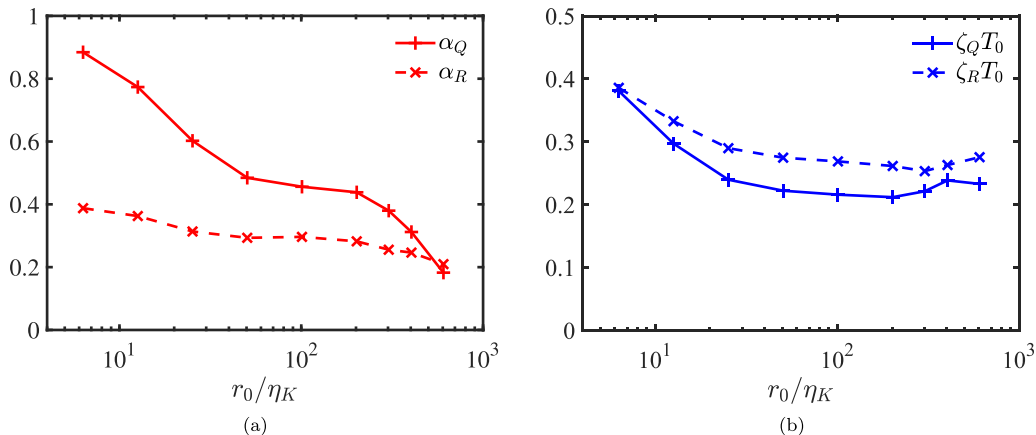
FIG. 2. The dimensionless model parameters determined from the slopes of the linear fitting in Fig. 1 (red dashed lines): (a) α and (b) ζT_0 as a function of scale r_0.

α or ζ terms in Eqs. (17) and (18). All quantities are nondimensionalized by T_0 and the size of the tetrahedra is $r_0 = 100\eta_K$. In all subfigures of Fig. 1, we plot the conditional averages of ordinates conditioned on abscissas, which are indicated by the black solid curves. One can see that in Figs. 1(a)–1(d), those black curves are very close to their linear fitting (the red dashed lines), except in Fig. 1(c), where it shows moderate deviation. From the fittings of the conditional means for tetrads by a linear dependence, consistent with Eqs. (23)–(26), one can determine the values of α and ζ (normalized by T_0) as a function of the size r_0. The result is shown in Fig. 2. The tetrad model postulates that the values determined from different relations should be close to each other. The discrepancy between α_R and α_Q, and between ζ_R and ζ_Q, indicates that the simple one-parameter model cannot accurately describe the full dynamics of $\hat{\mathbf{H}}$ ($\hat{\mathbf{H}}^p$ or $\hat{\mathbf{H}}^v$). The results in Fig. 2(a) show that when approaching the dissipative range, the discrepancy between α_Q and α_R becomes very large: α_Q grows to a value close to 1 in the dissipative range, which is due to the homogeneity constraint discussed in Ref. [29], while α_R is only ~ 0.4. On the other hand, in this work we are more interested in the inertial range, where these two values remain close to each other. In the inertial range, $\alpha_Q \sim 0.5$ and $\alpha_R \sim 0.3$, suggesting $\alpha \sim 0.4$ in the inertial range, which reflects a partial suppression effect on the nonlinearity. Meanwhile, $\zeta_Q \times T_0$ and $\zeta_R \times T_0$ are closer to each other, with $\zeta \times T_0 \sim 0.25$ in the inertial range as suggested by Fig. 2(b).

In Fig. 3 we further compare the α and ζ model terms with the pressure ($\hat{\mathbf{H}}^p$) and viscous ($\hat{\mathbf{H}}^v$) contributions to the exact dynamics at $t = 0$ by plotting their corresponding vector fields on the (R, Q) plane. The size of tetrahedra is $r_0 = 100\eta_K$, and the values of those parameters are determined from the algebraic average of the two curves in Fig. 2, i.e., α is chosen to be $(\alpha_Q + \alpha_R)/2 = (0.46 + 0.3)/2 = 0.38$ and $(\zeta_Q + \zeta_R)/2 = (0.22 + 0.27)/2 = 0.245$. The general observation from Fig. 3(a) is that the α model works well in two regions: around and beneath the Vieillefosse tail and the upper right corner of the plane (large positive Q and R); in other areas the model either underestimates the strength or misses the direction. While Fig. 3(b) shows that the behavior of the ζ model on the (R, Q) plane is quite close to $\hat{\mathbf{H}}^v$, except in the areas around strong negative Q and small R.

Figure 4 shows the $\hat{\mathbf{H}}$ term given by Eq. (13) (black arrows) and the two individual contributions due to pressure (green arrows) and viscosity (red arrows). One observes first that in certain parts of the (R, Q) plane, namely for large Q ($Q \times T_0^2 \gtrsim 5$), as well as along the line $\Delta = 0$, with positive R, the effects of pressure (green arrows) dominates viscosity (red arrows). In the rest of the (R, Q) plane, the influences of pressure and viscosity are comparable.
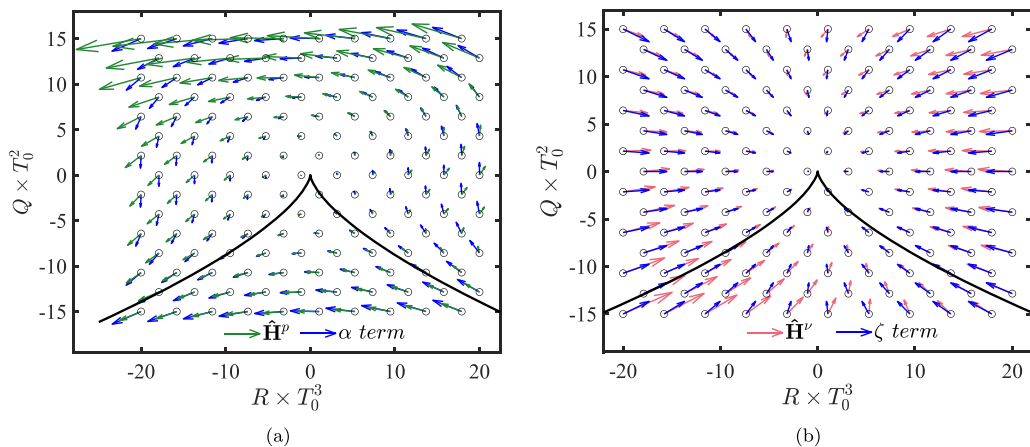
FIG. 3. Comparison between (a) the α model term and the contribution from the pressure term $\hat{\mathbf{H}}^p$ and (b) the ζ model term and the contribution from the viscous term $\hat{\mathbf{H}}^\nu$ on the invariants plane, $r_0 = 100\eta_K$ and time $t = 0$. The errors of the model with respect to real dynamics are $\sim$23% and $\sim$13% in (a) and (b), respectively, where the errors are calculated by $\Sigma|\mathbf{V_{real}} - \mathbf{V_{model}}|/\Sigma|\mathbf{V_{real}}|$, $\mathbf{V_{real}}$ and $\mathbf{V_{model}}$ denote the vectors of real dynamics and model predictions appear in the figure.

Figure 5 provides a direct comparison between the exact evolution, starting from a regular tetrad, with $r_0 \approx 100\eta_K$, as described by Eqs. (11) and (12) (red arrows) and the tetrad model approximation, Eqs. (18) and (17) (blue arrow). Overall, the tetrad model captures qualitatively the main features of the evolution. The comparison is particularly compelling below the separatrix, i.e., for $\Delta = 4Q^3 + 27R^2 \leqslant 0$, i.e., in strain dominated regions of the flow. For $\Delta > 0$, on the contrary, one observes a significant misalignment between the exact evolution equation and the tetrad-model prediction; namely the exact ev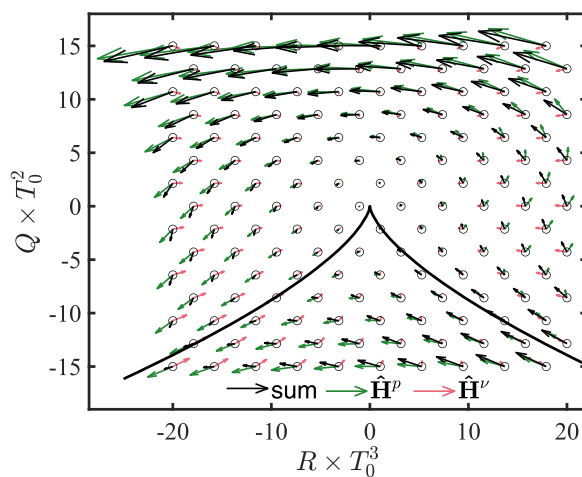olution tends to maintain the trajectories in the $R < 0$ regions more than the tetrad model. The tendency is reversed for $R > 0$.

FIG. 4. The pressure contribution $\hat{\mathbf{H}}^p$ (green), the viscous contribution $\hat{\mathbf{H}}^\nu$ (red), and the total $\hat{\mathbf{H}}$ term (black) to the dynamics in the (R, Q) plane. The contribution of the forcing term $\hat{\mathbf{H}}^f$ is not shown here since it is no more than a few percentages of $\hat{\mathbf{H}}$ on all points of the (R, Q) plane. The various terms are evaluated at $t = 0$ when the tetrahedra is regular, and the size is $r_0 \approx 100\eta_K$, well within the inertial range.
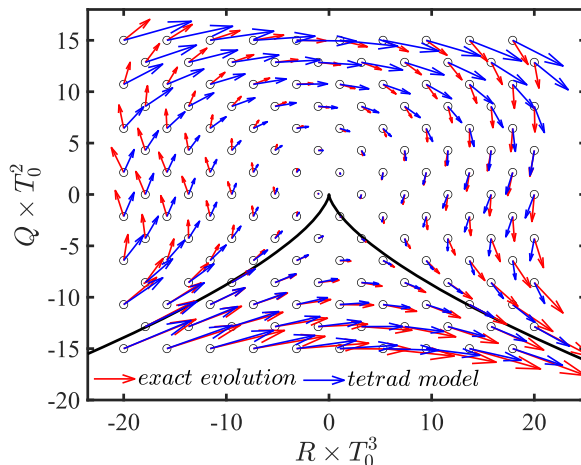
FIG. 5. Comparison of the velocity on the (R, Q) plane, $(dR/dt, dQ/dt)$, between the exact evolution equations for R and Q, Eqs. (11) and (12), and the tetrad model Eqs. (18) and (17). The velocities dR/dt and dQ/dt are constructed from regular tetrads, with $r_0 \approx 100\eta_K$.

The observation that the very short time dynamics of the flow differs qualitatively little from the expectation from the RE model is qualitatively consistent with the observed shape of the joint PDF of (R, Q) [7,19,20,30,31]. The longer-term dynamics, however, reveals a more complicated picture, discussed in the following subsection.

C. Short-time evolution on the (R, Q) plane

We now consider the dynamics over longer timescales. The data used in this section to construct the Lagrangian evolution of the PVGT are the dataset L, see Sec. III A.

Figure 6 shows the trajectories of the PVGT on the (R, Q) plane starting from initially regular tetrads of size $r_0 \approx 100\eta_K$ up to $t \approx 0.1\,T_0$ (red lines), together with the predictions from the tetrad model (blue lines). Note that the initial velocities of these trajectories are those given in Fig. 5,
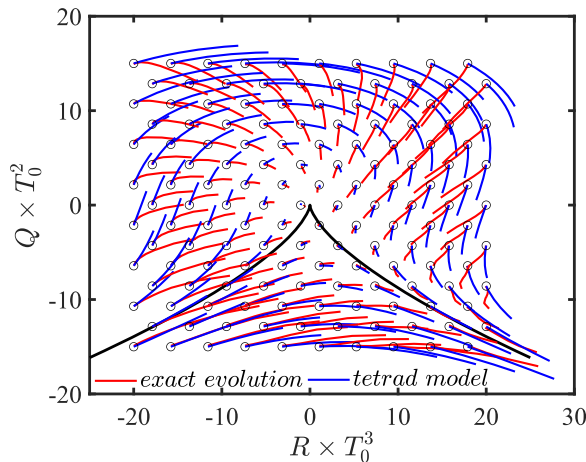

FIG. 6. Trajectories of initially isotropic tetrahedra with $r_0 \approx 100\eta_K$ in the (R, Q) plane. The red lines show the DNS data and the blue lines the prediction of the tetrad model over a duration $0.1\,T_0$.
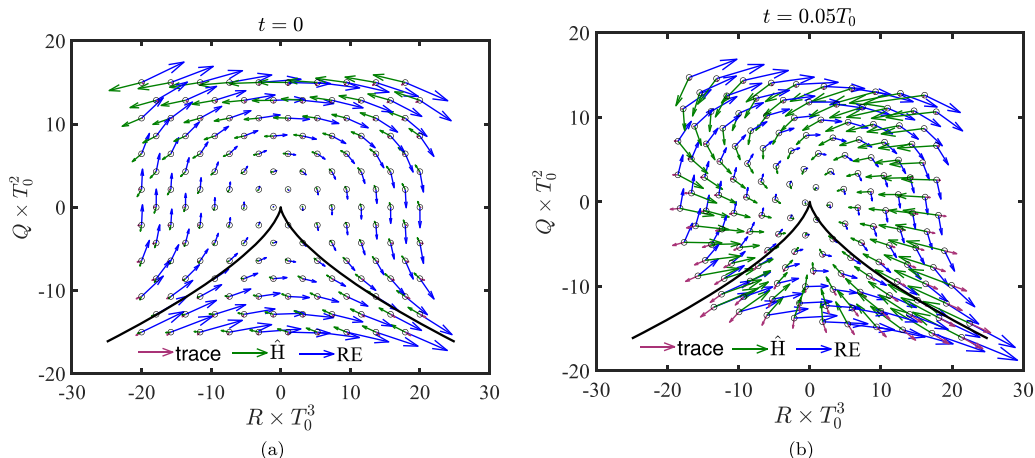
FIG. 7. The contributions to the dynamics in the (R, Q) plane from the trace term $-\frac{2}{3}\text{tr}(\mathbf{M})\hat{\mathbf{M}}$ (purple), the term $\hat{\mathbf{H}}$ (green), and the RE term $-\hat{\mathbf{M}}^2 + \frac{1}{3}\text{tr}(\hat{\mathbf{M}}^2)\mathbf{I}$ (blue) in Eq. (9) at times $t = 0$ and $t = 0.05T_0$. The size of the initially regular tetrahedra is $r_0 \approx 100\eta_K$.

which demonstrates that the tetrad model does provide a reasonable prediction at $t = 0$. Figure 6, however, shows that, even after a short time, $T_0/10 \approx 2.2\tau_K$, the trajectories predicted by the model and those from the DNS differ considerably in some parts of the (R, Q) plane. This is particularly the case in regions where vorticity dominates, well above the $\Delta = 0$ separatrix, where trajectories from the DNS turn towards the origin, $R = Q = 0$, while those predicted by the model follows the "streamlines" given by the initial velocity field shown in Fig. 5 because Eqs. (17) and (18) specify a "stationary flow pattern" on the (R, Q) plane if α and ζ are constant and the fluctuations are averaged out, and thus the Lagrangian trajectories coincide with the streamlines. By contrast, the dynamics does not change qualitatively much in the strain dominated regions or $\Delta \leqslant 0$.

The striking change of behavior revealed by Fig. 6 is unlikely to be attributable to the deformation of the tetrads, which occurs over a time of $\sim 0.2T_0$ (see Fig. 2 of Ref. [9]), longer than the duration of the trajectories shown in Fig. 6. The short timescale, $\sim 2\tau_K$, characterizing the change in the dynamics is rather reminiscent of the zero-crossing time of the Lagrangian autocorrelation of acceleration following fluid tracers [13,32–35]. In fact, acceleration and pressure gradient have been shown not to differ much from each other [36,37]. Moreover, we indeed observed that the decorrelation of the difference in the pressure gradient between two fluid tracers decays to zero at a time $\sim 2\tau_K$ (not shown), in which the shape deformation does not play any role.

Figure 7 shows the structure of the vector fields by comparing the contributions from the trace of the PVGT, $-\frac{2}{3}\text{tr}(\mathbf{M})\hat{\mathbf{M}}$, the unclosed term $\hat{\mathbf{H}}$, and the restricted Euler term $-\hat{\mathbf{M}}^2 + \frac{1}{3}\text{tr}(\hat{\mathbf{M}}^2)\mathbf{I}$ in Eq. (9) for the evolution of the PVGT from the DNS data. Panels 7(a) and 7(b) show the vectors at $t = 0$ and $t = 0.05T_0$, respectively, following the same set of tetrads. The vectors were obtained by conditional averages on the values of (R, Q) at the final time, so the starting points of the vectors on the two panels are not exactly the same. Remarkably, even after a very short time, $0.05T_0 \approx \tau_K$, the two vector fields in the (R, Q) plane on the two panels differ very much from each other, whereas at $t = 0$ the trace term is negligible; it becomes much more important at the later time, $t = 0.05 T_0$, particularly when $Q < 0$. Also, consistent with the findings of Fig. 6, the contribution of $\hat{\mathbf{H}}$ is directed towards the origin for $Q > 0$.

Further insight about the qualitative change in the dynamics is provided by Fig. 8, which shows the relative contributions of $\hat{\mathbf{H}}^p$ and $\hat{\mathbf{H}}^\nu$ to the dynamics at $t = 0.05T_0$ for the tetrads shown in Fig. 7. Figure 8 shows that at $t = 0.05T_0$, the pressure contribution dominates the viscosity term. The observations of Figs. 7 and 8 lead to the conclusion that, assuming that the formulation of the
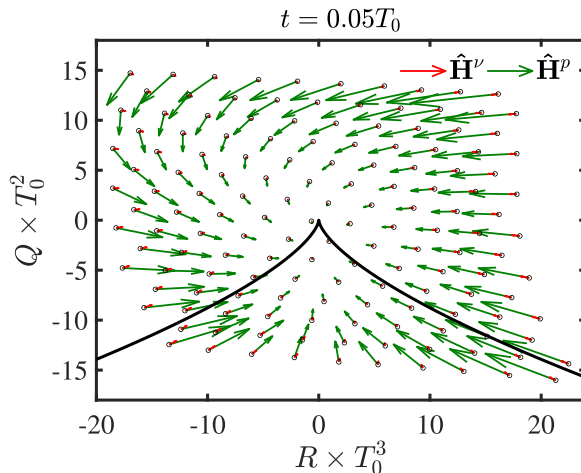
$$t = 0.05T_0$$

FIG. 8. Contributions to the dynamics in the (R, Q) plane of the pressure term $\hat{\mathbf{H}}^p$ (green) and the viscous term $\hat{\mathbf{H}}^\nu$ (red) at $t = 0.05T_0$ for initially regular tetrads with size $/r_0 \approx 100\eta_K$.

closure of the $\hat{\mathbf{H}}$ term in terms of α and ζ remains valid, the precise values of the parameters must change very rapidly. To test this hypothesis, we determined the instantaneous values of α and ζ from the DNS data, by computing the conditional averages of dR/dt, dQ/dt on (R, Q) and then least-squares fitting with Eqs. (17) and (18). The results are shown in Fig. 9 for t up to $\sim 0.1T_0$.

For all four sets of tetrads with different initial sizes, the values of α go down rapidly from its initial value ~ 0.5 towards zero, while ζT_0 increases from ~ 0 to ~ 1. Interestingly, the time of evolution of α, rescaled by T_0 in Fig. 9(a), appears to superpose relatively well except for tetrads with the smallest initial size, $r_0/\eta_K \approx 25$. This discrepancy is likely due to the fact that $r_0 = 25\eta_K$ is not fully in the inertial range of scales. On the other hand, the evolution of ζT_0 seem to superpose better when scaling t by τ_K, see Fig. 9(b), particularly for $r_0/\eta_K \approx 100$ (squares) and 200 (diamonds). For the sake of comparison, the inset of the Fig. 9(b) shows the dependence of ζT_0 as a function of t/T_0.

With the caveat that the two timescales T_0 and τ_K do not differ very much from each other over the range of scales considered here ($0.1T_0 \approx 3.4\tau_K$ for $r_0/\eta_K = 200$), the results above suggest that the
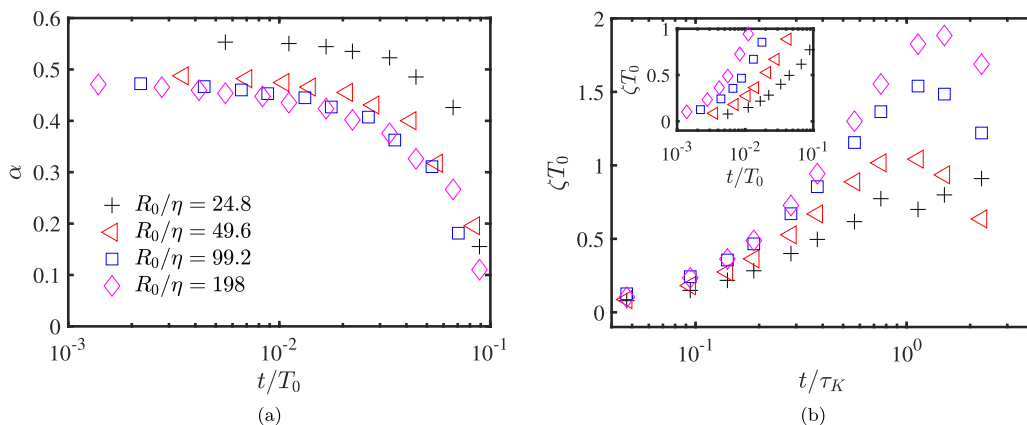

FIG. 9. Least-squares fitting for parameters (a) α and (b) ζT_0 by comparing the exact dynamics and model predictions on the (R, Q) invariants plane up to $t \approx 0.1T_0$, for $r_0 \approx 25\eta_K$ (the black "plus" symbols), $r_0 \approx 50\eta_K$ (red triangle symbols), $r_0 \approx 100\eta_K$ (blue square symbols), and $r_0 \approx 200\eta_K$ (magenta diamond symbols).
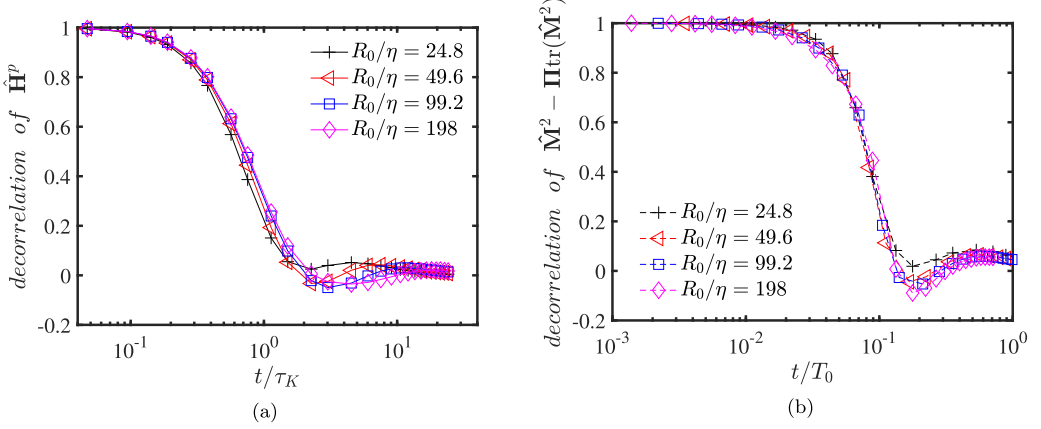
FIG. 10. $\langle Y(0)Y(t)\rangle/\langle Y(0)^2\rangle$ with (a) $Y = \hat{\mathbf{H}}^p$ and (b) $Y = \hat{\mathbf{M}}^2 - \mathbf{\Pi} \mathrm{tr}(\hat{\mathbf{M}}^2)$, for $r_0 \approx 25\eta_K$ (black "plus" symbols), $r_0 \approx 50\eta_K$ (red triangles), $r_0 \approx 100\eta_K$ (blue squares), and $r_0 \approx 200\eta_K$ (magenta diamonds).

dynamics of $\mathbf{M}$ involves not only T_0 but also τ_K. As another example of this behavior, Fig. 10 shows how much $\hat{\mathbf{H}}^p$ [Fig. 10(a)], and $\alpha[\hat{\mathbf{M}}^2 - \mathbf{\Pi} \, \mathrm{tr}(\hat{\mathbf{M}}^2)]$ [Fig. 10(b)] are correlated with their values at $t = 0$. The former decorrelates over a characteristic time $\sim\tau_K$, which is also the decorrelation time of the acceleration fluctuations [13,32,33,35]. The model term, by contrast, rather seems to decay over a characteristic timescale $\sim T_0$. This result could imply that while some quantities evolve at the characteristic timescale corresponding to the scale r_0 of the tetrad, other quantities may in fact relax much faster, with a characteristic time τ_K. As the ratio T_L/τ_K grows only linearly with R_λ, it will be difficult to shed much light on these issues, even with the largest numerical simulations available.

D. Fluctuation around the mean

As explained in Sec. II B, one way to model the variability of the unclosed terms in Eq. (9) from tetrad-to-tetrad consists in introducing a noise term, namely $\boldsymbol{\eta}$ in Eq. (15), which generates fluctuations of the trajectories as a function of time. To characterize these fluctuations, we compute the variance of $\Delta R(t) \equiv R(t) - R(0)$ and $\Delta Q(t) \equiv Q(t) - Q(0)$, which quantifies the spread of the trajectories on the (R, Q) plane over a time interval t. In fact, Eqs. (17) and (18) lead to an explicit prediction for the growth of the variance of the fluctuations of R and Q:

$$\mathrm{var}(\Delta Q(t)) = C_\eta \frac{\varepsilon}{r_0^2} \langle \mathrm{tr}(\hat{\mathbf{M}}\hat{\mathbf{M}}^{\mathbf{T}}) \rangle t, \tag{27}$$

$$\mathrm{var}(\Delta R(t)) = C_\eta \frac{\varepsilon}{r_0^2} \left\langle \mathrm{tr}(\hat{\mathbf{M}}^2(\hat{\mathbf{M}}^{\mathbf{T}})^2) - \frac{1}{3}\mathrm{tr}(\hat{\mathbf{M}}^2)^2 \right\rangle t, \tag{28}$$

in which C_η is a dimensionless constant. The simple dependence in t in Eqs. (27) and (28) results from the fact that the noise has been postulated in Eq. (15) to be white-in-time. This form can only be an approximation, aimed at describing the behavior for inertial scales, and nominally for scales such that $T_0 \equiv (r_0^2/\epsilon)^{1/3} \gg \tau_K$. However, the behavior of the underlying Navier-Stokes dynamics is expected to be smooth on a timescale of order τ_K. Furthermore, as already noticed, the integral and the Kolmogorov timescales are not so different over the range of scales considered here: $T_0/\tau_K = (r_0/\eta)^{1/3}$, a ratio that does not exceed ~ 4.7 for $r_0 = 100\eta_K$.

In fact, the DNS results reveal a more complicated behavior. Figures 11(a) and 11(b) show the variances of ΔR and ΔQ as a function of t/τ_K, in which the variances were compensated by the expressions given by Eqs. (27) and (28) such that a plateau corresponds to the constant C_η, independent of the scale r_0 and of the Reynolds number. Figures 11(a) and 11(b) show that at times shorter than $\sim\tau_K$, $\mathrm{var}(\Delta R(t))$ and $\mathrm{var}(\Delta Q(t))$ both grow, essentially $\propto t^2$. This behavior at very
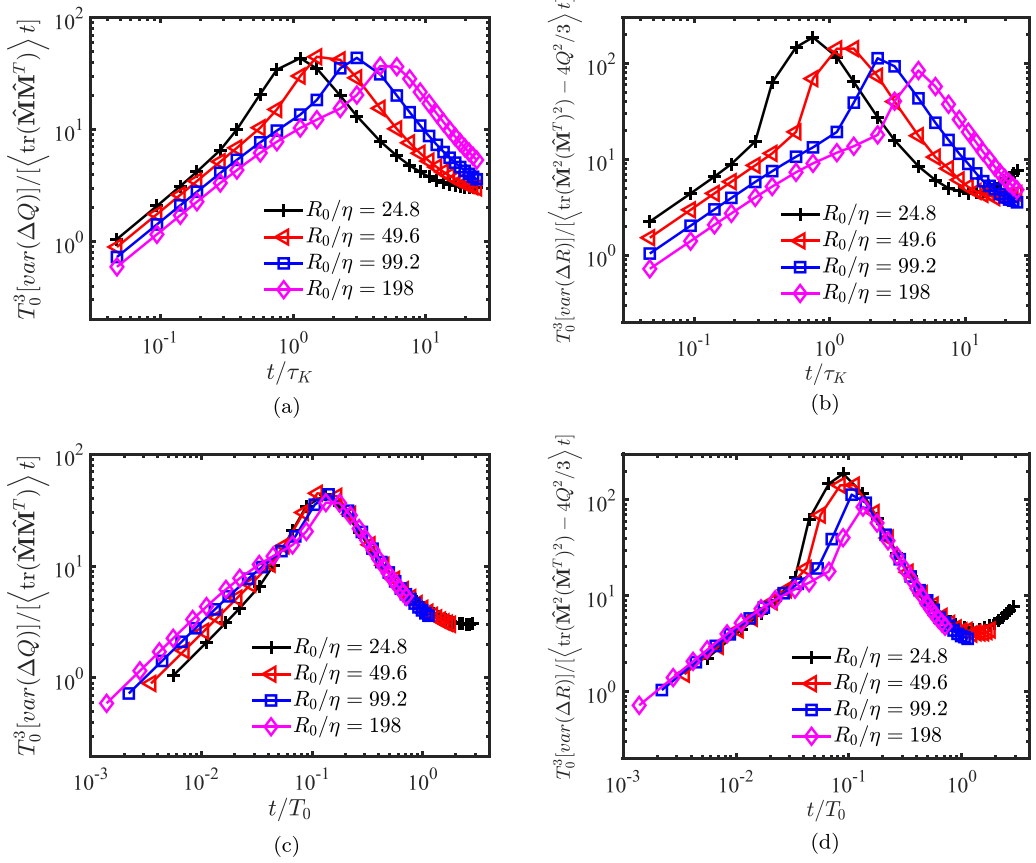
FIG. 11. The growth of the variance of the Q and R divided by $\langle \mathrm{tr}(\hat{\mathbf{M}}\hat{\mathbf{M}}^{\mathrm{T}}) \rangle \times t/T_0^3$ [(a) and (c)] and divided by $\langle \mathrm{tr}(\hat{\mathbf{M}}^2(\hat{\mathbf{M}}^{\mathrm{T}})^2) - 4Q^2/3 \rangle \times t/T_0^3$ [(b) and (d)], respectively for four different sizes of tetrahedra. The horizontal axis is normalized by τ_K in panels (a) and (b) and by T_0 in panels (c) and (d); it is clear that T_0 is a better choice for collapsing curves from different r_0.

short times merely reflects the fact that the postulated white-in-time functional form for the noise in Eq. (16) is inappropriate at very short time, where the various functions are smooth in time. We notice, however, that the time at which the curves start deviating from the $\propto t^2$ behavior depend on r_0, when plotted as a function of t/τ_K. To explore further this issue, Figs. 11(c) and 11(d) show the same quantities, with time rescaled by T_0. These curves reveal a much better collapse as a function of r_0. These observations, consistent with those of Fig. 10, suggest a subtle decorrelation of the subgrid terms, not reducible to Eq. (16). Also, the lack of any evidence for the formation of a plateau in the curves shown in Fig. 11 points to a more serious deviation from the expectation based on Eqs. (27) and (28).

IV. CONCLUSIONS

In this work, we studied the short-time evolution of the PVGT constructed from four fluid tracers initially forming regular tetrahedra. To this end, we projected the dynamics on the plane of the invariant (R, Q). With the help of DNS data, we compared the model terms introduced in the tetrad model [7] with the exact evolution equations. In qualitative agreement with earlier studies, we found that at very short times, the tetrad model reproduces many qualitative features of the dynamics,

including the role of the pressure in partial depletion of the nonlinear terms of the equations, and the damping behavior of the viscous term. On the other hand, the prediction of the tetrad model that the depression of nonlinearity affects equally the R and Q dynamics turns out to be quantitatively incorrect. This provides a hint that the assumption, consisting of modeling the pressure Hessian by the simple α-term in Eq. (15), is insufficient.

The dynamics at longer times, up to $t \approx 0.1T_0$, where T_0 is the turbulent eddy-turnover timescale corresponding to the initial size of the tetrads, reveals an even more dramatic change in the dynamical behavior. Whereas the trajectories on the (R, Q) plane, underneath the separatrix $4Q^3 + 27R^2 = 0$ (the "Vieillefosse tails"), remain close to the model prediction, the trajectories above the separatrix, in vorticity-dominated regions strongly deviate from the predictions and turn towards the origin $(R, Q) = (0, 0)$, with a very fast decorrelation timescale, approximately of the order of the Kolmogorov timescale τ_K. Importantly, this observation indicates that even the short-time evolution of PVGT cannot be understood by Taylor expanding the dynamics at $t = 0$. Specifically, the results of Fig. 10 suggest that the decorrelation time of the unclosed terms related to $\hat{\mathbf{H}}$ is τ_K, while the decorrelation time of the model terms related to $\hat{\mathbf{M}}$ is likely to be T_0. Our work therefore suggests that the Kolmogorov timescale, τ_K, should be explicitly taken into account when modeling the evolution of the PVGT. This would be essential for predicting, for example, the tumbling dynamics of slender rods in turbulence [38].

Finally, the white-in-time and Gaussian noise assumptions of the fluctuation around the mean evolution of $\hat{\mathbf{M}}$ does not capture very well the fluctuations of the dynamics. In particular, DNS data suggests that the timescale of the fluctuation is closer to the eddy turn over time at scale r_0, $T_0 = (r_0^2/\varepsilon)^{1/3}$. The discrepancies between the DNS results and the predictions of the tetrad model highlights the difficulty in modeling the pressure Hessian along Lagrangian trajectories. The strong qualitative difference between strain-dominated regions [below the separatrix in the (R, Q) plane] and vorticity-dominated regions point to important differences in the evolution of the pressure Hessian, depending on the precise structure of the velocity gradient. Investigating these issues is the key to understand Lagrangian dynamics of turbulence.

As a perspective, we remark that the approach presented here can be tested using experimental data from particle tracking measurements, as in Ref. [9]. In this regard, the most recent algorithms [39] make it possible to follow accurately very large sets of tracers, allowing us to test the ideas developed in this work in various flow configurations, potentially at much larger Reynolds numbers than considered here. The accurate measurement of the pressure gradients and/or pressure Hessian, however, remains a major experimental challenge, although recent progress has been made, leading to a compelling determination of the single-particle statistics [40–42].

[1] C. Meneveau, Lagrangian dynamics and models of the velocity gradient tensor in turbulent flows, Annu. Rev. Fluid Mech. **43**, 219 (2011).

[2] V. Borue and S. A. Orszag, Local energy flux and subgrid-scale statistics in three-dimensional turbulence, J. Fluid Mech. **366**, 1 (1998).

[3] F. van der Bos *et al.*, Effects of small-scale turbulent motions on the filtered velocity gradient tensor as deduced from holographic particle image velocimetry measurements, Phys. Fluids **14**, 2456 (2002).

[4] B. Tao, J. Katz, and C. Meneveau, Statistical geometry of subgrid-scale stresses determined from holographic particle image velocimetry measurements, J. Fluid Mech. **457**, 35 (2002).

[5] M. Carbone and A. D. Bragg, Is vortex stretching the main cause of the turbulent energy cascade ? J. Fluid Mech. **883**, R2 (2020).

[6] P. L. Johnson, Energy Transfer from Large to Small Scales in Turbulence by Multi-Scale Nonlinear Strain and Vorticity Interaction, Phys. Rev. Lett. **124**, 104501 (2020).

[7] M. Chertkov, A. Pumir, and B. I. Shraiman, Lagrangian tetrad dynamics and the phenomenology of turbulence, Phys. Fluids **11**, 2394 (1999).

[8] H. Xu, A. Pumir, and E. Bodenschatz, The pirouette effect in turbulent flows, Nat. Phys. **7**, 709 (2011).

[9] A. Pumir, E. Bodenschatz, and H. Xu, Tetrad deformation and alignment of perceived vorticity and strain in a turbulent flow, Phys. Fluids **25**, 035101 (2013).

[10] A. Pumir, B. I. Shraiman, and M. Chertkov, Geometry of Lagrangian Dispersion in Turbulence, Phys. Rev. Lett. **85**, 5324 (2000).

[11] L. Biferale, G. Boffetta, A. Celani, B. J. Devenish, A. Lanotte, and F. Toschi, Multiparticle dispersion in fully developed turbulence, Phys. Fluids **17**, 111701 (2005).

[12] H. Xu, N. T. Ouellette, and E. Bodenschatz, Evolution of geometric structures in intense turbulence, New J. Phys. **10**, 013012 (2008).

[13] J. F. Hackl, P. K. Yeung, and B. L. Sawford, Multi-particle and tetrad statistics in numerical simulations of turbulent relative dispersion, Phys. Fluids **23**, 065103 (2011).

[14] A. N. Kolmogorov, The local structure of turbulence in incompressible viscous fluid for very large Reynolds numbers, Dokl. Akad. Nauk SSSR **30**, 301 (1941).

[15] U. Frisch, *Turbulence: The Legacy of A. N. Kolmogorov* (Cambridge University Press, Cambridge, UK, 1995).

[16] P. Vieillefosse, Local interaction between vorticity and shear in a perfect incompressible fluid, J. Phys. France **43**, 837 (1982).

[17] P. Vieillefosse, Internal motion of a small element of fluid in an inviscid flow, Physica A **125**, 150 (1984).

[18] B. J. Cantwell, Exact solution of a restricted Euler equation for the velocity gradient tensor, Phys. Fluids A **4**, 782 (1992).

[19] B. J. Cantwell, On the behavior of velocity gradient tensor invariants in direct numerical simulations of turbulence, Phys. Fluids A **5**, 2008 (1993).

[20] H. M. Blackburn, N. N. Mansour, and B. J. Cantwell, Topology of fine-scale motions in turbulent channel flow, J. Fluid Mech. **310**, 269 (1996).

[21] L. Chevillard and C. Meneveau, Lagrangian Dynamics and Statistical Geometric Structure of Turbulence, Phys. Rev. Lett. **97**, 174501 (2006).

[22] L. Chevillard, C. Meneveau, L. Biferale, and F. Toschi, Modeling the pressure hessian and viscous laplacian in turbulence: Comparisons with direct numerical simulation and implications on velocity gradient dynamics, Phys. Fluids **20**, 101504 (2008).

[23] P. F. Yang, A. Pumir, and H. Xu, Dynamics and invariants of the perceived velocity gradient tensor in homogeneous and isotropic turbulence, J. Fluid Mech. **897**, A9 (2020).

[24] B. J. Devenish, Geometrical Properties of Turbulent Dispersion, Phys. Rev. Lett. **110**, 064504 (2013).

[25] M. Wilczek and C. Meneveau, Pressure Hessian and viscous contributions to velocity gradient statistics based on Gaussian random fields, J. Fluid Mech. **756**, 191 (2014).

[26] J. Martin, A. Ooi, C. Dopazo, M. S. Chong, and J. Soria, The inverse diffusion time scale of velocity gradients in homogeneous isotropic turbulence, Phys. Fluids **9**, 814 (1997).

[27] Y. Li, E. Perlman, M. Wan, Y. Yang, C. Meneveau, R. Burns, S. Chen, A. Szalay, and G. L. Eyink, A public turbulence database cluster and applications to study lagrangian evolution of velocity increments in turbulence, J. Turbul. **9**, N31 (2008).

[28] H. Yu, K. Kanov, E. Perlman, J. Graham, E. Frederix, R. Burns, A. Szalay, G. Eyink, and C. Meneveau, Studying Lagrangian dynamics of turbulence using on-demand fluid particle tracking in a public turbulence database, J. Turbul. **13**, N12 (2012).

[29] Z. D. Zhou and P. F. Yang, Homogeneity constraints on the mixed moments of velocity gradient and pressure Hessian in incompressible turbulence, Phys. Rev. Fluids **8**, 024601 (2023).

[30] J. Martin, A. Ooi, M. S. Chong, and J. Soria, Dynamics of the velocity gradient tensor invariants in isotropic turbulence, Phys. Fluids **10**, 2336 (1998).

[31] A. Pumir and A. Naso, Statistical properties of the coarse-grained velocity gradient tensor in turbulence: Monte-Carlo simulations of the tetrad model, New J. Phys. **12**, 123024 (2010).

[32] N. Mordant, A. M. Crawford, and E. Bodenschatz, Experimental lagrangian acceleration probability density function measurement, Physica D **193**, 245 (2004).

[33] P. K. Yeung and S. B. Pope, Lagrangian statistics from direct numerical simulations of isotropic turbulence, J. Fluid Mech. **207**, 531 (1989).

[34] P. K. Yeung, S. B. Pope, E. A. Kurth, and A. G. Lamorgese, Lagrangian conditional statistics, acceleration and local relative motion in numerically simulated isotropic turbulence, J. Fluid Mech. **582**, 399 (2007).

[35] G. Falkovich, H. Xu, A. Pumir, E. Bodenschatz, L. Biferale, G. Boffetta, A. S Lanotte, and F. Toschi, On lagrangian single-particle statistics, Phys. Fluids **24**, 055102 (2012).

[36] P. Vedula and P. K. Yeung, Similarity scaling of acceleration and pressure statistics in numerical simulations of isotropic turbulence, Phys. Fluids **11**, 1208 (1999).

[37] D. Buaria and K. R. Sreenivasan, Scaling of Acceleration Statistics in High Reynolds Number Turbulence, Phys. Rev. Lett. **128**, 234502 (2022).

[38] N. Pujara, G. A. Voth, and E. A. Variano, Scale-dependent alignment, tumbling and stretching of slender rods in isotropic turbulence, J. Fluid Mech. **860**, 465 (2019).

[39] A. Schröder and D. Schantz, 3D Lagrangian particle tracking in fluid mechanics, Annu. Rev. Fluid Mech. **55**, 511 (2023).

[40] Z. Wang, Q. Gao, C. Wang, R. Wei, and J. Wang, An irrotation correction on pressure gradient and orthogonal-path integration for PIV-based pressure reconstruction, Exp. Fluids **57**, 104 (2016).

[41] Y. Lin and H. Xu, Divergence–curl correction for pressure field reconstruction from acceleration in turbulent flows, Exp. Fluids **64**, 137 (2023).

[42] Y. Lin and H. Xu, Experimental investigation of pressure statistics in laboratory homogeneous isotropic turbulence, Phys. Fluids **35**, 065129 (2023).